ADVANCED HEALTHCARE MATERIALS
www.advhealthmat.de

Monoclonal Antibody-Guided Tumor-Targeted Hollow Virus-Like Cerium Oxide with Oxygen Self-Supply for Intensifying Photodynamic Therapy

Mengqi Li, Jiajing Liu, Xian Luo, Zhiyu Zhao, Shengyu Wang, Zongjunlin Liu, Tingting Li, Dong Yang, Yang Li, Peiyuan Wang,* Fanghong Luo,* and Jianghua Yan**

The hypoxic character of tumors and the poor targeting ability of photosensitizers often limit the efficacy of photodynamic therapy (PDT). In recent years, the discovery of metal nanoenzymes and nanocarriers has improved PDT. Thereby, to improve the effective utilization of photosensitizers and oxygen (O_2) in tumors, herein, a nanosystem (LS-HB@HvCeO$_2$-NRP1 mAb, LHCN1) is reported, in which a hollow virus-like cerium oxide (HvCeO$_2$) is surface-decorated with tumor-targeting neuropilin-1 monoclonal antibody (NRP1 mAb), and loaded with a photosensitizer (chlorin e6-C-15-ethyl ester, LS-HB). In vitro and in vivo experiments demonstrate that LHCN1 can efficiently accumulate within the tumor sites via the targeting guidance of NRP1 mAb and is then rapidly endocytosed into cells. Furthermore, HvCeO$_2$ with catalase-mimetic activity can decompose the endogenous hydrogen peroxide (H_2O_2) to promote O_2 via the valence transformation between Ce^{4+} and Ce^{3+}, relieving tumor hypoxia and improving the PDT efficacy. Upon near-infrared laser irradiation, LS-HB produces large amounts of cytotoxic reactive oxygen species. Moreover, LHCN1 is used in fluorescence/photoacoustic multimodal imaging for in vivo drug localization, and its use in PDT evidently helps inhibit tumor growth with no apparent toxicity to normal tissues. Thus, LHCN1 may provide a promising strategy for precise tumor-specific diagnosis and treatment.

1. Introduction

Photodynamic therapy (PDT), a new non-invasive diagnosis and treatment method suitable for various tumor therapies, is appealing with a few side effects, repeatable treatment, less trauma, good selectivity, and wide applicability.[1] After laser irradiation, a photosensitizer (PS) can transfer energy to triplet oxygen, which can be converted into singlet oxygen ($^1O_2$). As a type of reactive oxygen species (ROS), $^1O_2$ can directly destroy nucleic acids, proteins, lipids, and other macromolecules related to cell structure and function, killing tumor cells via autophagy, scorch death, apoptosis, and necrosis.[2] Furthermore, the mitochondrial pathway is one of the mechanisms by which PDT promotes apoptosis.[3] According to the previous reports, three basic elements are required for PDT: laser irradiation, oxygen (O_2), and PS.[4] At present, there are three generations of PSs. Compared with the first generation (such as haematoporphyrin derivatives), the second-generation PSs (such as 5-aminolevulinic acid derivatives and dihydroporphyrin derivatives) have many advantages, such as stronger tissue penetration, higher $^1O_2$ yield, notably enhanced utilization, better selectivity, lower toxicity and fewer side effects, and high chemical purity.[1b,5] However, most of second-generation PSs have poor water solubility and low delivery efficiency, and the affinity of drugs to tumor has not been improved.[6] Chlorin e6-C-15-ethyl ester (LS-HB) is dihydroporphyrin e6-c15-ethyl ester and second-generation PSs that can be activated by near-infrared (NIR) laser at 660 nm and has better water solubility than other second-generation PSs. Moreover, LS-HB notably possesses self-luminous characteristic,[7] providing the basis for its use as a fluorescent probe.

However, the poor targeting ability of PSs and their rapid in vivo metabolism limit the antitumor effect of PDT.[8] Tumor-targeting and -responsive carriers are needed to achieve the precise release of PSs. Neuropilin-1 monoclonal antibody (NRP1 mAb) has excellent affinity for neuropilin-1 (NRP1) expressed highly in various tumors, such as oesophageal cancer,[9] can be used to improve the tumor-targeting efficacy of carriers. Moreover, there are currently various tumor responsive nanocarriers, such as tumor acidic microenvironment-responsive nanomaterials, tumor $^1O_2$- and hypoxia-responsive pharmaceutical micelles, exhibit good drug delivery and enhance antitumor effects.[10]

M. Li, J. Liu, X. Luo, Z. Zhao, S. Wang, Z. Liu, T. Li, D. Yang, F. Luo, J. Yan
Cancer Research Center
School of Medicine
Xiamen University
Xiamen 36100, P. R. China
E-mail: luofanghong@xmu.edu.cn; jhyan@xmu.edu.cn
Y. Li, P. Wang
Key Laboratory of Design and Assembly of Functional Nanostructures
Fujian Institute of Research on the Structure of Matter
Chinese Academy of Science
Fuzhou 350007, P. R. China
E-mail: li.yang@fjirsm.ac.cn; wangpeiyuan@fhirsm.ac.cn

The ORCID identification number(s) for the author(s) of this article can be found under https://doi.org/10.1002/adhm.202202418

DOI: 10.1002/adhm.202202418

Those provided a powerful reference measure for improving drug targeted-tumor delivery. However, owing to the hypoxic state in most solid tumor cells, the efficacy of O_2-dependent PDT is hindered.[11] Currently, many studies have intensively explore strategies for improving PDT efficiency.[10a,12] Moreover, endogenous hydrogen peroxide (H_2O_2) content in most solid tumors is 10–100 μM, significantly higher than that in normal cells, providing a feasible pathway for alleviating the lack of O_2 in tumors with the assistance of catalase.[13] In recent years, metal nanoenzymes have become a popular research field because of their good enzyme-like activity. Although parts of nanoenzymes, such as iron oxide and tricobalt tetroxide, can simulate catalase, their biocompatibility problems have been encountered.[14] Cerium oxide (CeO_2), one of the metal nanoenzymes, is widely used as a catalyst with low side effects.[15] In the natural environment, CeO_2 is a mixture of tri-(Ce^{3+}) and tetravalent (Ce^{4+}) Ce, which can be transformed into each other.[16] The representation of enzyme-like activity mainly depends on the proportion of Ce^{4+} and Ce^{3+} in CeO_2,[13b] which is affected by pH, synthesis strategy, and CeO_2 nanoparticles size.[17] On the one hand, when the proportion of Ce^{3+} is higher than that of Ce^{4+}, the enzyme activity is mainly superoxide dismutase mimetic activity.[15d,18] On the other hand, when the proportion of Ce^{4+} is higher than that of Ce^{3+}, CeO_2 mainly displays catalase-mimetic activity, decomposing H_2O_2 to produce O_2 and water molecules.[13b,19] Therefore, designing a degradable and efficient CeO_2 that acts as a catalase mimic to alleviate the hypoxia in tumor cells and increase the O_2 source for PDT has important significance for PDT.

In this study, based on the second-generation PSs, we designed a novel virus-like catalase-mimetic nanoparticle to improve the efficacy of PDT by effective O_2 self-supply in tumor and precise delivery of LS-HB to tumor tissues. First, we prepared the virus-inspired mesoporous silica nanoparticles (VMSi) as a hard template. Thereafter, nanoscale CeO_2 was coated on the roughened surface of the VMSi to successfully obtain a novel hollow virus-like mesoporous CeO_2 ($HvCeO_2$) with both carrier and enzyme functions. To enhance the tumor cell targeting capability, NRP1 mAb was utilized to anchor the roughened $HvCeO_2$ surface ($HvCeO_2$-NRP1 mAb, abbreviated as HCN1) to specifically bind to NRP1 overexpressed on the membrane of tumor cell membranes. Finally, we encapsulated LS-HB within HCN1 to construct a novel LS-HB@$HvCeO_2$-NRP1 mAb nanoparticle (LHCN1). 48 h post-injection, LHCN1 was still capable of accumulating efficiently in the tumor tissue. After tumor cells endocytosed LHCN1, Ce^{4+} reacted with intracellular endogenous H_2O_2 in tumor cells to produce O_2 to alleviate hypoxia. When exposed to 660 nm near-infrared laser irradiation, LS-HB was activated to produce a large amount of ROS from O_2 to induce apoptosis and necrosis of cells for PDT. Meanwhile, our LHCN1 presented negligible systematic toxicity during treatment, revealing great potential for translation in the PDT of clinical solid tumors (**Scheme 1**).

2. Results and Discussion

2.1. Characterization of LHCN1

A schematic of LHCN1 fabrication is shown in **Figure 1**A. First, the virus-like mesoporous VMSi with a rough surface and spinous tubes was fabricated according to a previously reported via water/oil bi-phase reaction system.[20] Tetraethyl orthosilicate (TEOS) dispersed in cyclohexane was added to the surface of water with hexadecyl trimethyl ammonium bromide (CTAB) and NaOH. After the silica precursor (TEOS) dispersed in cyclohexane reacting with CTAB and NaOH for 72 h on the water surface, the morphology of the obtained nanoparticles was similar to that of spherical viruses with spikes, and it was confirmed by transmission electron microscopy (TEM) and field emission scanning electron microscopy (SEM; Figure 1B-i,v). The VMSi nanoparticles had uniform size and excellent monodispersity, with diameters of ≈127.6 nm (Figure S1a, Supporting Information). Second, the hollow virus-like $HvCeO_2$ was synthesized using the hard template method. CeO_2 was deposited and coated on the etched VMSi nanoparticles; after 24 h of reaction, the template was almost etched under this weak alkali system, enabling $HvCeO_2$ to be obtained. The TEM and SEM images showed that $HvCeO_2$ retained the viral shape, and its diameter increased to 138.9 nm, confirming the successful synthesis of $HvCeO_2$ (Figure 1B-ii,vi, and Figure S1b, Supporting Information). Moreover, the X-ray powder diffraction (XRD) spectra showed only a single broad diffraction peak at $2\theta = 25°$, indicating that the as-made $HvCeO_2$ nanoparticles were amorphous structure (Figure 1D). Compared with the previously reported Ce-based nano-enzyme, the amorphous structure indicated that $HvCeO_2$ was amenable to degradation. In addition, the specific surface area of $HvCeO_2$ was measured to be 223.5846 $m^2\ g^{-1}$ based on the N_2 desorption branch of the isotherm and the Barrett–Joyner–Halenda method. The relationship between pore diameter and dV/dD pore volume indicated that the pore tubes of $HvCeO_2$ were bimodal mesopores with the average diameters of 4 and 6.4 nm, indicating the stacking pores formed by CeO_2 nanoparticles and the mesoporous tubes of VMSi nanoparticles, respectively (Figure 1C). The large specific surface area provided an adequate basis for the efficient loading of LS-HB. Next, the amino groups were functionalized on $HvCeO_2$ via 3-aminopropyl triethoxysilane (APTES) hydrolysis, and the NRP1 monoclonal antibody (NRP1 mAb) was anchored on the particle surface via the EDC/NHS reaction ($HvCeO_2$-NRP1 mAb, HCN1). HCN1's size (≈166.3 nm) was determined using dynamic light scattering (DLS; Figure S1c, Supporting Information). Interestingly, the stretching vibration absorption peaks of LHCN1 and NRP1 mAb at 3277, 1640, and 1531 cm^{-1} in Fourier transform infrared spectrometer (FTIR) spectra confirmed that NRP1 mAb and $HvCeO_2$ were bound by an amide bond (Figure 1E). SEM and TEM images verified the successful surface modification of NRP1 mAb on $HvCeO_2$ (Figure 1B-iii,vi). Moreover, fluorescence spectrophotometry showed that LHCN1-RBITC [rhodamine B 5-isothiocyanate (RBITC) labeling NRP1 mAb] retained the fluorescence absorption peaks at 595 nm, the wavelength of RBITC (Figure 1G). Based on Table S1, Supporting Information, we analyzed the NRP1 mAb loading rate, which was ≈8.09%. Subsequently, LS-HB molecules were loaded into LHCN1 cavity. The loading efficiency of LS-HB of LHCN1 was calculated to be ≈14%. In addition, ultraviolet–visible (UV–vis) NIR spectrophotometry showed that LHCN1 had UV–vis characteristic absorption peaks of LS-HB at wavelengths of ≈660 and 400 nm (Figure 1F). These results demonstrated that NRP1 mAb and LS-HB of LHCN1 were successfully loaded. Moreover, energy dispersive spectroscopy (EDS) images revealed the dark-field

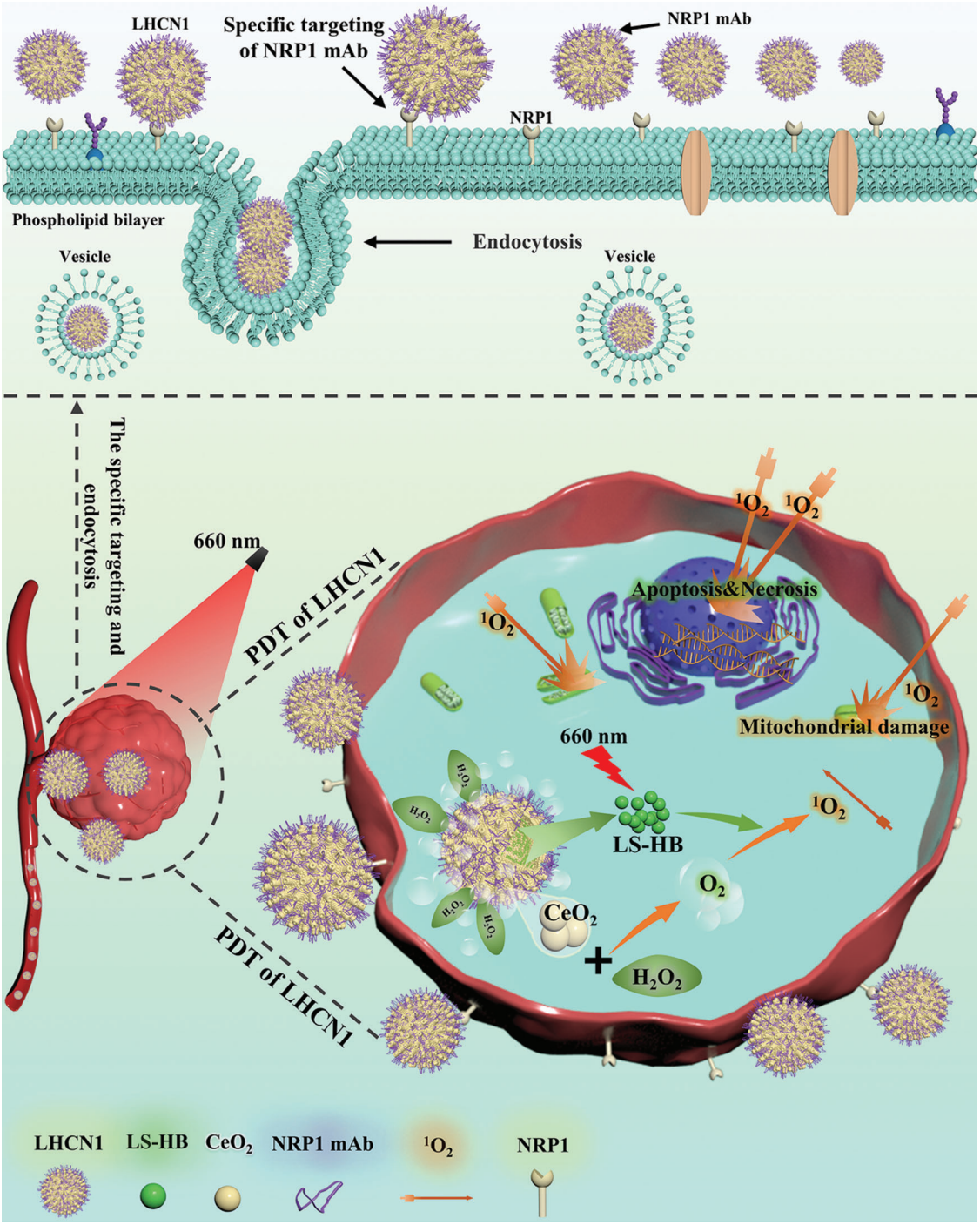

Scheme 1. Schematic illustration of tumor cytomembrane highly expressed NRP1-targeting virus-like LHCN1 for intensifying PDT and killing tumor cells via self-supplying O_2.

(DF) and high-angle annular dark-field (HAADF) LHCN1 morphology and that LHCN1 contained C/N/O/Ce/Si elements (Figure 1B-iv,viii,H). The N element was derived from the NRP1 mAb in LHCN1, and the Si element should be assigned to the framework of LHCN1. DLS analyzed LHCN1's diameter distribution, and the size was ≈173.4 nm (Figure S1d, Supporting Information). Furthermore, EDS also verified that the hollow nanoparticles were prepared successfully. Moreover, the electric potential of amino modified $HvCeO_2$ ($HvCeO_2$-NH_2) was 6.94 mV. Subsequently, the charge was transformed to the negative charge (−26.03 mV) after $HvCeO_2$-NH_2 was modified by NRP1 mAb. Finally, the −19.17 mV electric potential of LHCN1 explained the loading of LS-HB (Figure S2, Supporting Information). The changes in zeta electric potentials also illustrated the successful

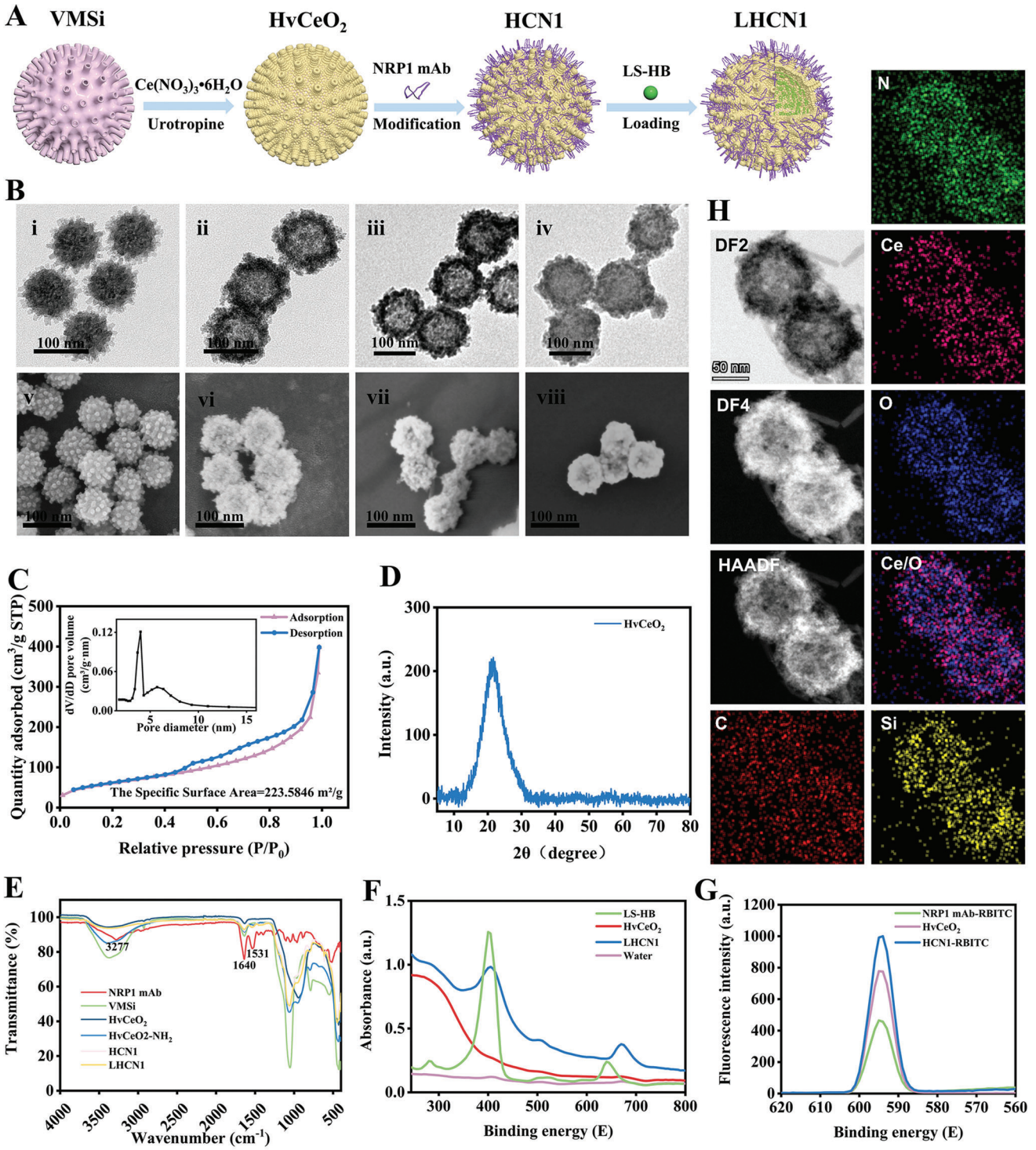

Figure 1. Characterization of $HvCeO_2$ and LHCN1. A) Schematic diagram of VMSi, $HvCeO_2$, HCN1, and LHCN1. B) TEM images of i) VMSi, ii) $HvCeO_2$, iii) HCN1, and iv) LHCN1, and SEM images of v) VMSi, vi) $HvCeO_2$, vii) HCN1, and viii) LHCN1. Scale bar: 100 nm. C) N_2 adsorption–desorption isotherm and BJH desorption d*V*/d*D* pore volume of $HvCeO_2$. D) XRD pattern of $HvCeO_2$. E) FTIR of NRP1 mAb, VMSi, $HvCeO_2$, $HvCeO_2$-NH_2, HCN1, and LHCN1. F) UV–vis spectra of LS-HB, $HvCeO_2$, and LHCN1. G) Fluorescence spectra of NRP1 mAb, $HvCeO_2$, and HCN1. H) DF2, DF4, HAADF images and EDS element mappings of LHCN1. Scale bar: 50 nm.

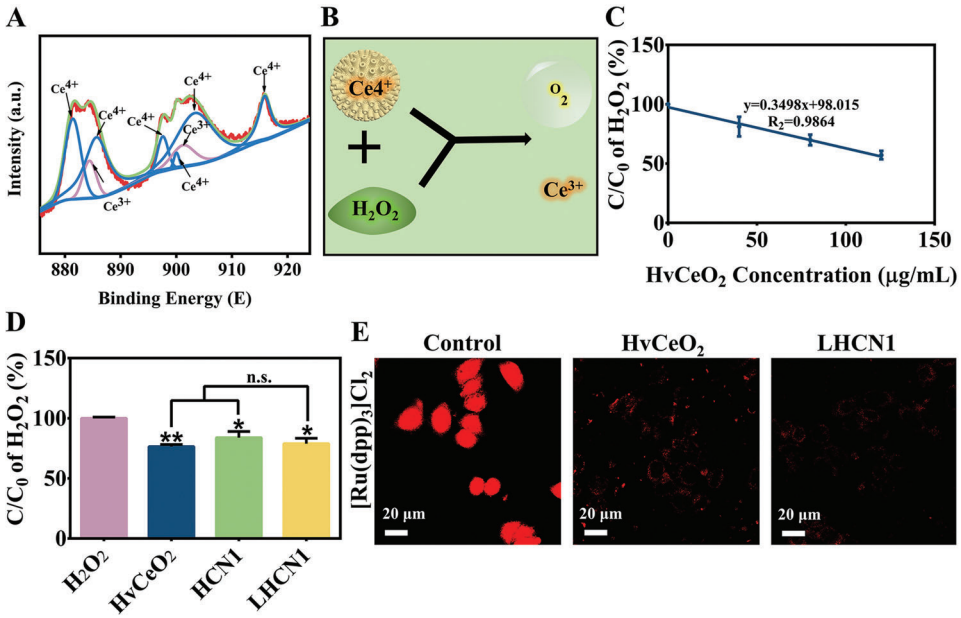

Figure 2. The evaluation of catalase-mimetic activity of CeO_2. A) XPS spectrum of Ce valence state of $HvCeO_2$. B) Schematic diagram of catalase-mimetic activity of Ce^{4+}. C) Catalase-mimetic activity of $HvCeO_2$ evaluated at different concentrations (C/C_0: the actual residual H_2O_2 percentage based on the initial H_2O_2 concentration; mean ± SD, $n = 3$). D) The evaluation of catalase-mimetic activity of $HvCeO_2$, HCN1, and LHCN1 (all three containing the same $HvCeO_2$ concentration; mean ± SD, $n = 3$, $*p < 0.05$, $**p < 0.01$). E) CLSM images for the detection of O_2 generation in human esophageal cancer (MMP-2) cells incubated with $HvCeO_2$ and LHCN1. Scale bar: 20 μm.

modification of NRP1 mAb and PS loading. These results were consistent with those of UV–vis spectroscopy and EDS, further proving the reliability of our experimental methods for constructing of LHCN1.

2.2. Hypoxia Alleviation Performance of LHCN1

CeO_2 mainly acts as a catalase-mimetic agent to decompose H_2O_2 when the proportion of Ce^{4+} is higher than that of Ce^{3+}.[19a] The chemical valence state analysis of Ce in LHCN1 by X-ray photoelectron spectroscopy (XPS) showed that Ce in LHCN1 was in a mixed valence state and that the content of Ce^{4+} was much higher than that of Ce^{3+}—the ratio of Ce^{3+} to Ce^{4+} was 1/5.6 (**Figure 2**A). Therefore, LHCN1 could mimic catalase activity. Figure 2B demonstrates the process by which Ce^{4+} decomposed H_2O_2 to produce O_2. To further demonstrate whether CeO_2 nanoparticles could stimulate catalase to decompose H_2O_2 or not, the H_2O_2 content detection kit was used to detect H_2O_2 consumption. As shown in Figure S3, Supporting Information, the H_2O_2 consumption gradually increased with time in three pHs, and faster decomposing rate was found in the neutral pH than that in other two pHs. Interestingly, after $HvCeO_2$-treatment 120 min, H_2O_2 consumption in three acid-incubated $HvCeO_2$ were apparent, and the actual residual H_2O_2 percentage [expressed as (C/C_0)%] were 64.28%, 60.56%, and 55.43% in pHs 5.5, 6.5, and 7.4, respectively. Those indicated that $HvCeO_2$ had a superior ability to decompose H_2O_2 for O_2 generation in the cytoplasm of the tumor cells. Moreover, as shown in Figure 2C, H_2O_2 was consumed gradually with increasing $HvCeO_2$ concentration. In addition, HCN1 and LHCN1 maintained the catalase-mimetic activity to decompose H_2O_2, demonstrating that photosensitizers loading and antibodies modification had insignificant effects on the H_2O_2 decomposition abilities of CeO_2 (Figure 2D). The intracellular O_2 generation was evaluated by confocal laser scanning microscopy (CLSM) after the cells were treated with $HvCeO_2$ and LHCN1. Compared with the conspicuous red fluorescence of $[Ru(dpp)_3]Cl_2$ of the control group, negligible fluorescence signals were detected in the HCN1 and LHCN1 groups because O_2 produced in cells treated with HCN1 and LHCN1 quenched the fluorescence of $[Ru(dpp)_3]Cl_2$ (Figure 2E). The above results showed that $HvCeO_2$, HCN1, and LHCN1 could act as catalase mimics to provide sufficient O_2 for PDT in cells.

2.3. In Vitro Compatibility of LHCN1 and the Targeting Ability of NRP1 mAb and Intracellular Uptake

Cell Viability Detection Kit (CCK-8) could conveniently and accurately detect cell viability to analyze cell proliferation and drug toxicity. As shown in **Figure 3**A, the viability of normal human oesophageal epithelial cells (Het-1a) showed no obvious difference and remained at ≈90% after treatment with different concentrations of LHCN1 for 12 and 24 h. This implied that LHCN1 nanoparticles were biocompatible with normal human oesophageal epithelial cells. The MMP-2 cell viabilities were above 80% after treated with within 80 μg mL^{-1} LHCN1 and HCN1 for 12 and 24 h. In addition, although MMP-2 cells were treated with different concentrations of LS-HB, HCN1, and LHCN1, the dark toxicity to cells was low, and was not different from that of the control group (Figure 3B). In previous studies, NRP1 proteins were found on the membrane of oesophageal

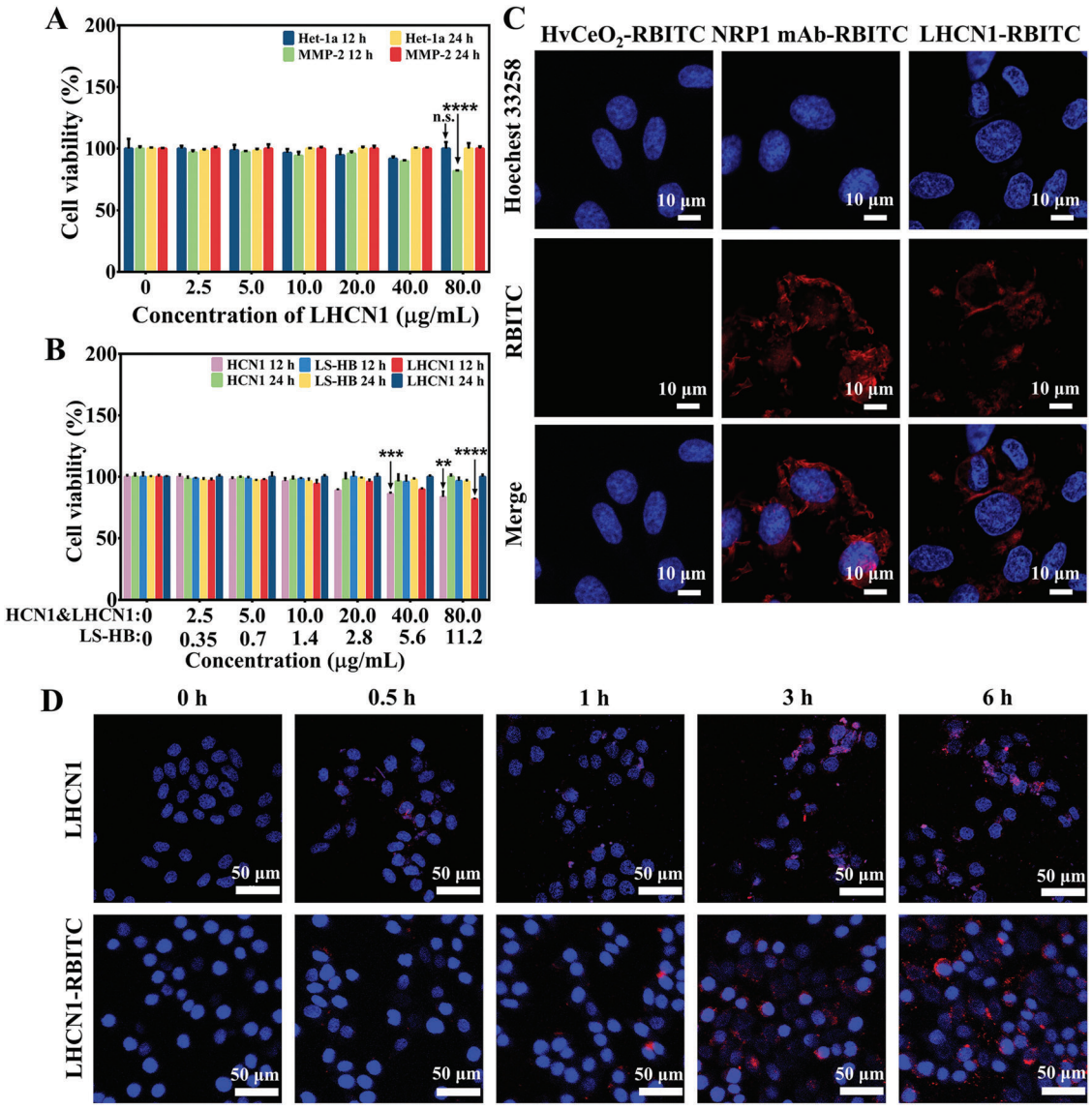

Figure 3. The in vitro compatibility of LHCN1 and the in vitro targeting ability of NRP1 mAb and intracellular uptake. A) The cell viability of Het-1a and MMP-2 cells treated with LHCN1 for 12 and 24 h (mean ± SD, $n = 3$, $^{****}p < 0.0001$). B) The cell viability of MMP-2 cells treated with HCN1, LS-HB, and LHCN1 (the concentration of contained LS-HB consistent with that in the LS-HB group) at different concentrations for 12 and 24 h (mean ± SD, $n = 3$, $^{**}p < 0.01$, $^{***}p < 0.001$, $^{****}p < 0.0001$). C) The targeting ability evaluation of RBITC-labeled NRP1 mAb and RBITC-labeled LHCN1 for 0.5 h using a CLSM. Scale bar: 10 μm. D) CLSM images of MMP-2 cells incubated with LHCN1 and RBIRC-labeled LHCN1 for 0, 0.5, 1, 3, and 6 h. Scale bar: 50 μm.

cancer cells and were specifically bound by NRP1 mAb.[9] Encouraged by the outstanding biocompatibility of LHCN1, the endocytosis and targeting ability of LHCN1 toward MMP-2 cells were imaged by a CLSM. The fluorescence of LS-HB and RBITC could be probed at 660 and 590 nm wavelengths using a CLSM, respectively. Interestingly, the CLSM imaging results revealed that NRP1 mAb and LHCN1 (all NRP1 mAb was labeled with RBITC) were concentrated on the cell membranes when cells were incubated with NRP1 mAb-RBITC and LHCN1-RBITC for 0.5 h. In contrast, no obvious red fluorescence was observed on the cytomembrane after cells were incubated with RBITC-labeled $HvCeO_2$ for the same co-culture time (Figure 3C). Significantly, these findings demonstrated that the targeting ability of NRP1 mAb to oesophageal cancer cells and that LHCN1 maintained the comparable targeting ability to that of NRP1 mAb. When LS-HB was used as a fluorescent probe, LHCN1 nanoparticles were endocytosed gradually into the cytoplasm of MMP-2 cells after 0.5 h co-incubation, while the content of incubated LHCN1 tended to reach the saturation state after co-incubation for 3 h (Figure 3D and Figure S4, Supporting Information). The similar results were obtained when RBITC was used as a fluorescent probe and labeled NRP1 mAb (Figure 3D), proving the active targeting and drug delivery capability of our novel $HvCeO_2$-based nanoenzyme.

2.4. In Vitro Photodynamic Effect of LHCN1

To explore the PDT effect of LHCN1, we first explored the effect of NRP1 mAb on the MMP-2 cell viability via CCK-8 detection and found that the MMP-2 cell viability was above 90% after treatment with 11.2 μg mL^{-1} NRP1 mAb for 12 and 24 h, demonstrating the nontoxicity of NRP1 mAb to MMP-2 within this concentration range (Figure S5, Supporting Information). In addition, contrary to the findings that the toxicity to gastric cancer and breast cancer cells occurred when NRP1 mAb reached a specific high concentration, 11.2 μg mL^{-1} was within the safe concentration range.[9d,e] Combined with the above experimental results on the targeting ability of LHCN1, we found that the NRP1 mAb of LHCN1 mainly played the role of targeting tumors in this study. We then evaluated the cellular killing effect of LHCN1 under 660 nm laser irradiation. **Figure 4**A shows that the inhibition of cells viability in the LHCN1 + Laser group was evidently stronger than that in the LS-HB + Laser group at the equal concentrations of LS-HB, and that the average viability (3.4%) of MMP-2 treated with 40 μg mL^{-1} LHCN1 and 5 J cm^{-2} laser irradiation was significantly lower than that (13.3%) of MMP-2 treated with 5.6 μg mL^{-1} LS-HB and 5 J cm^{-2} laser irradiation. Subsequently, the cell apoptosis following LHCN1 + Laser treatment was determined using Annex v/FITC assay. The results showed that, following 660 nm laser irradiation, the average apoptosis rates induced by low, medium, and high concentrations of LHCN1 were 12.2%, 38.9%, and 91.0%, respectively (Figure 4B,C), demonstrating that the extent of cell apoptosis depended on the concentration of LHCN1, basically consistent with the results shown in Figure 4A. Moreover, the average apoptosis rate following treatment with 40 μg mL^{-1} LHCN1 was 1.17-fold higher than that following treatment with 5.6 μg mL^{-1} (77.7%). Finally, living and dead cells discrimination was conducted using AM/PI staining (Figure 4D). The number of the dead cells in the LHCN1 + Laser group was markedly higher than that in the other groups, and the results were consistent with those observed by optical microscopy (Figure S6, Supporting Information). Moreover, after laser irradiation, optical microscopy revealed that LHCN1-treated tumor cells showed cell membranes bubbling or "germination," cell swelling, and nuclear pyknosis. Those were the morphological changes of apoptosis and necrosis, respectively. The number of apoptotic and necrotic cells in the LHCN1 + Laser group was higher than that in the LS-HB + Laser group. Thus, LHCN1 nanoparticles could promote apoptosis and necrosis of oesophageal tumor cells without toxicity to normal esophageal epithelium after 660 nm laser irradiation. The photodynamic effect induced by LHCN1 was more remarkable than that of LS-HB, which further illustrated that HCN1 could improve the photodynamic effect of LS-HB by combining HCN1's characteristics of tumor-targeting and O_2 supplying.

2.5. Detection of Intracellular ROS and the Change in Mitochondrial Membrane Potential

Based on the findings that LHCN1 + Laser treatment could cause apoptosis and necrosis in a large number of cells and the basic principle of PDT that PSs promote ROS production after laser irradiation at a specific wavelength to kill tumor cells, we determined ROS generation using DCFH-DA, a general indicator of oxidative stress. DCFH-DA could be hydrolyzed to produce 2′,7′-dichlorodihydrofluorescein (DCFH) by cellular esterase after entering cells, after which ROS oxidized DCFH to produce the strongly fluorescent product 2′,7′-dichlorofluorescein (DCF). The green fluorescence of DCF was detected using a CLSM with the laser excitation of 488 nm. **Figure 5**A shows almost no green fluorescence in the only laser, only drug, and control groups. The ROS produced in the LHCN1 + Laser group were significantly higher than those produced in the LS-HB + Laser group, meanwhile, the fluorescence intensity of ROS generation also displayed concentration-dependent behavior after laser irradiation. In other words, the fluorescence intensity of cells treated with 40 μg mL^{-1} LHCN1 showed predominantly higher ROS production in the cytoplasm. It could be seen from the flow cytometry results (Figure 5B,C) that the fluorescence intensity of the LHCN1 + Laser group was more than twice that of the LS-HB + Laser group, which was consistent with the results of CLSM imaging. The above results demonstrated that the laser irradiation activation of the LS-HB of LHCN1at 660 nm could trigger photodynamic effect that produced the highest levels of ROS in tumor cells. The depolarization of the mitochondrial membrane potential was a characteristic change in early apoptosis.[21] The JC-1 staining assay was used to determine the effect of LHCN1 on the changes in mitochondrial membrane potential. The red fluorescence indicated that JC-1 accumulated in mitochondria and formed JC-1 aggregates, while the green fluorescence indicated that JC-1 monomers did not bind to the mitochondrial inner membrane and retained in the cytoplasm, signifying the mitochondrial membrane potential depolarization. As depicted in Figure 5D, only laser irradiation or LHCN1 did not significantly affect changes in the mitochondrial membrane potential. In contrast, relative to the other treatments, the green fluorescence was remarkably higher after MMP-2 cells were treated with LHCN1 and laser (660 nm, 5 J cm^{-2}) irradiation, and the apparent mitochondrial membrane potential depolarization occurred. These findings indicated that PDT of LHCN1 could elevate the level of ROS, affect tumor cells by affecting mitochondria, and even promote cell apoptosis.

2.6. In Vivo distribution and the O_2-generating capability of LHCN1

Based on the previous reports, LS-HB can be used as a fluorescent probe.[22] The in vivo distribution of LHCN1 was evaluated using real-time intravital fluorescence imaging system. **Figure 6**A shows that LS-HB most markedly accumulated at the tumor site 6 h after intravenous injection and then gradually decreased, which was attributed to the ease of metabolizing the small molecule LS-HB. In contrast, LS-HB@$HvCeO_2$ ($HvCeO_2$ loading LS-HB) remained relatively stronger fluorescence at the tumor site 24 h post-injection, which was attributed to the enhanced permeability and retention effect of macromolecule $HvCeO_2$ nanoparticles on tumor capillaries and cells. After LHCN1 was injected into tumor-bearing mice, the fluorescence at the tumor site gradually increased over time. Furthermore, LHCN1 was mainly enriched at the tumor site 12 h post-injection, and the tumor site significantly remained strong fluorescence at

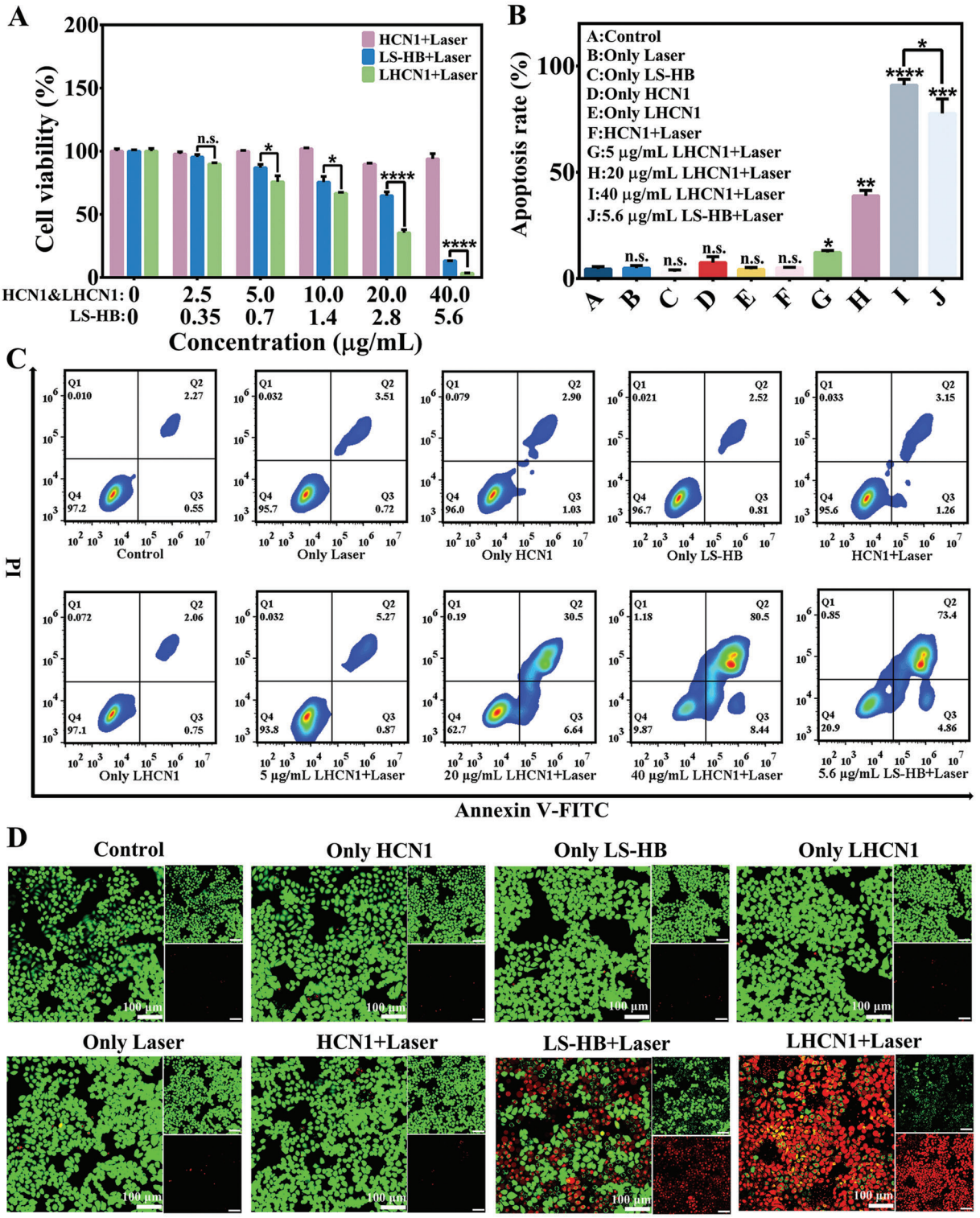

Figure 4. In vitro photodynamic effect of LHCN1. A) The viability of MMP-2 cells treated with HCN1, LS-HB, and LHCN1 (the concentration of contained LS-HB consistent with that of the LS-HB group) at different concentrations following 5 J cm^{-2} laser irradiation (mean ± SD, $n = 3$, $^{*}p < 0.05$, $^{****}p < 0.0001$). B,C) Flow cytometry analysis and statistics of the apoptosis of MMP-2 cells treated with HCN1, LS-HB, and LHCN1 following 5 J cm^{-2} laser irradiation, (A) Control, (B) only laser, (C) only LS-HB, (D) only HCN1, (E) only LHCN1, F: HCN1 + laser, G: 5 μg mL^{-1} LHCN1 + laser, H: 20 μg mL^{-1} LHCN1 + laser, I: 40 μg mL^{-1} LHCN1 + laser (containing 5.6 μg mL^{-1} LS-HB), J: 5.6 μg mL^{-1} LS-HB + laser (mean ± SD, $n = 3$, $^{*}p < 0.05$, $^{**}p < 0.01$, $^{***}p < 0.001$, $^{****}p < 0.0001$). D) CLSM images of MMP-2 cells stained with Calcein AM/PI following different treatments (the concentration of contained LS-HB of the LHCN1 group consistent with that of the LS-HB group; the laser intensity: 5 J cm^{-2}). Scale bar: 100 μm.

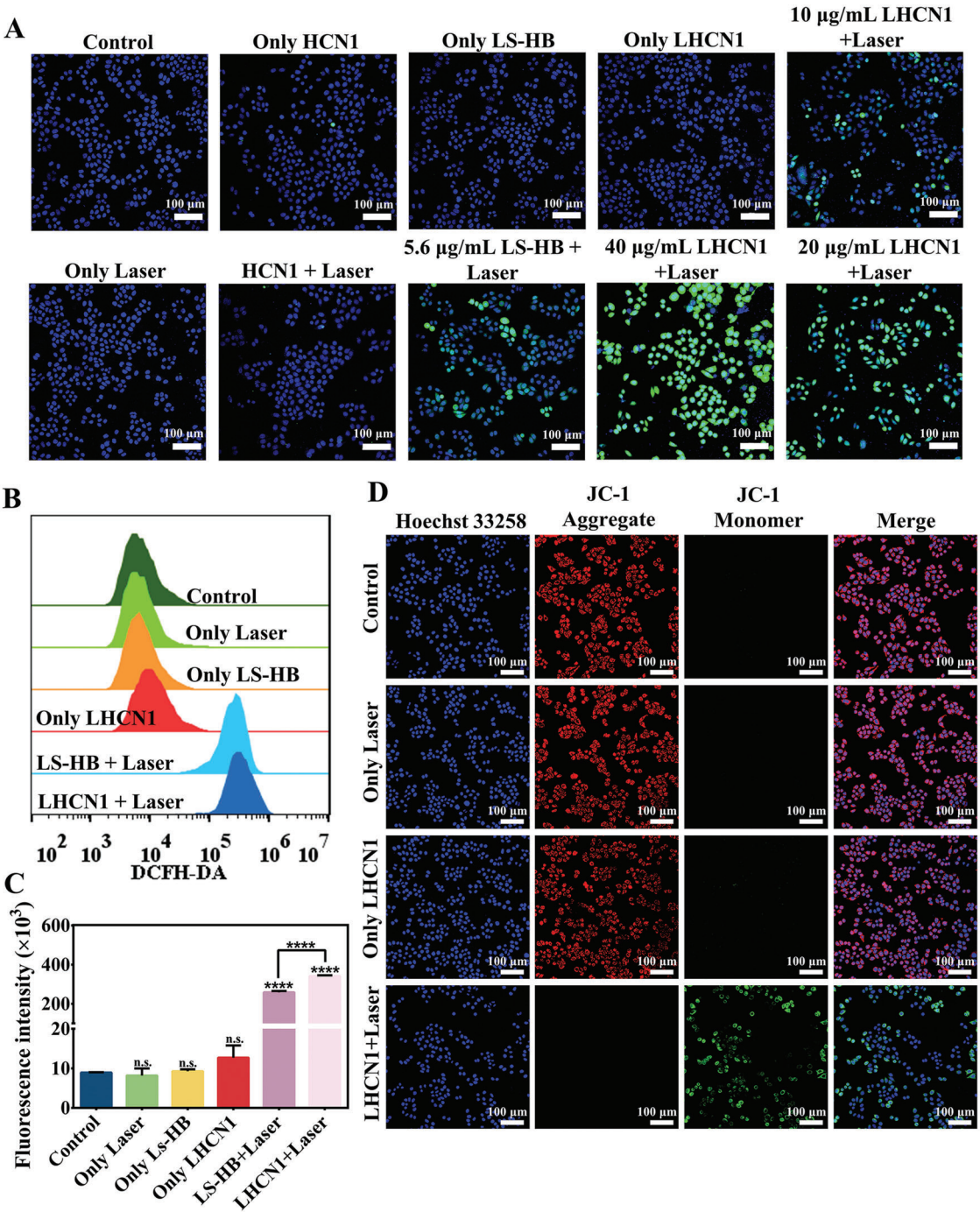

Figure 5. The in vitro detection of ROS and the changes of mitochondrial membrane potential. A) CLSM images of MMP-2 cells stained with DCFH-DA after different treatment (40 μg mL^{-1} LHCN1 containing 5.6 μg mL^{-1} LS-HB). Scale bar: 100 μm. B,C) Flow cytometry analysis of fluorescence intensity of MMP-2 cells stained with DCFH-DA following MMP-2 cells treated with 5 J cm^{-2} laser, LS-HB, HCN1, LS-HB + 5 J cm^{-2} laser, and LHCN1 + 5 J cm^{-2} laser. Data were expressed as mean ± SD, $n = 3$, ****$p < 0.0001$. D) CLSM images of MMP-2 cells stained with JC-1 following different treatment. Scale bar: 100 μm.

48 h post-injection, higher than elsewhere in the body and the LS-HB and LS-HB@$HvCeO_2$ groups, indicating the effective tumor-targeting capability of NRP1 mAb. The imaging of each group's dissected heart, liver, spleen, lung, kidney, brain, skin, muscle, and tumors further showed that LHCN1 nanoparticles had the most efficient tumor-site accumulation ability at 48 h compared with LS-HB and LS-HB@$HvCeO_2$ (Figure 6B,C). The photoacoustic (PA) imaging system displayed the similar results after LHCN1 injection (Figure 6D). The above results demonstrated the tumor-targeting ability and the long-term tumor

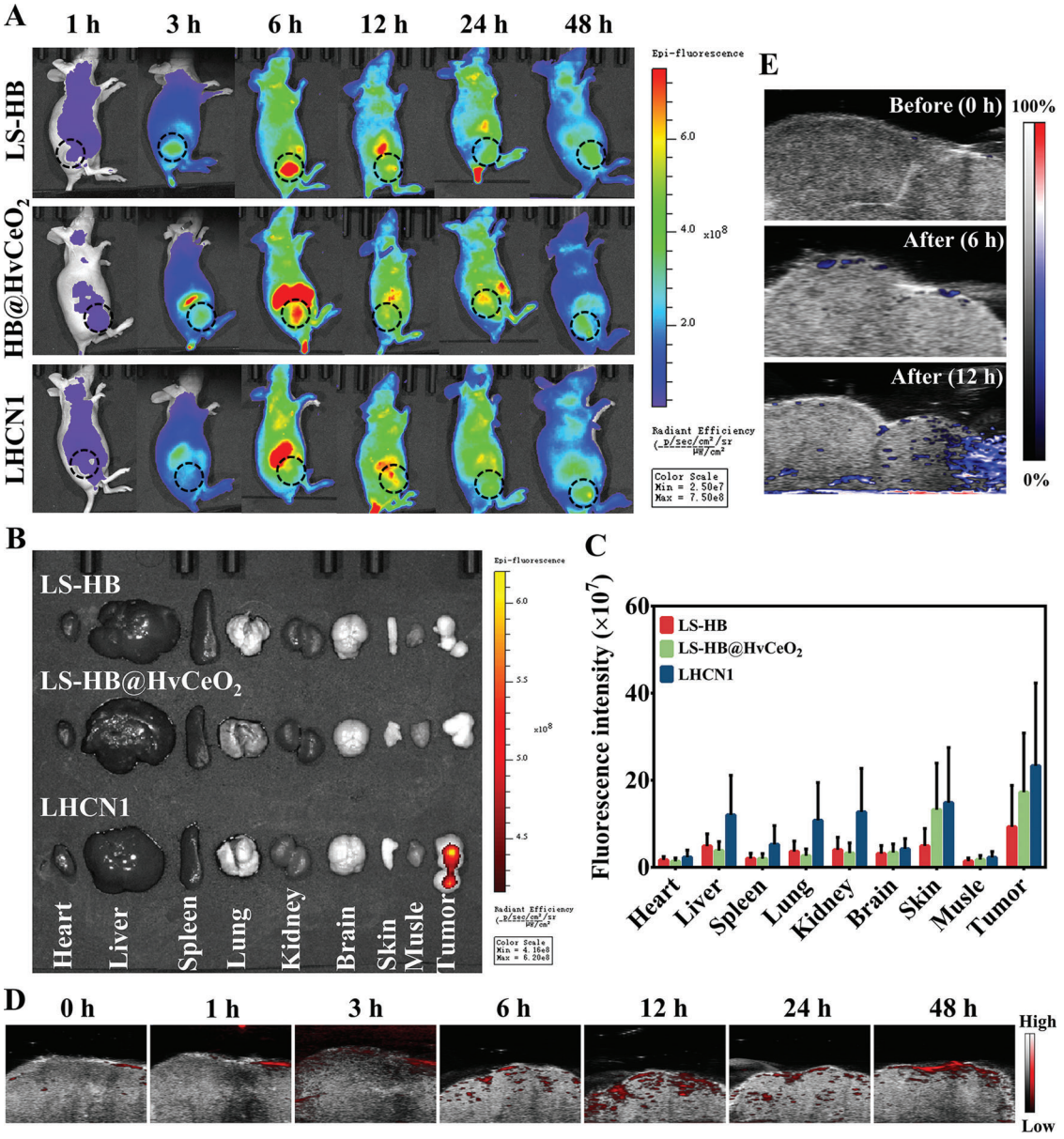

Figure 6. In vivo distributions of drugs at different time. A) The fluorescent imaging of tumor-bearing mice at 1, 3, 6, 12, 24, and 48 h after caudal vein injection of LS-HB, LS-HB@HvCeO$_2$, and LHCN1. B,C) Ex vivo fluorescent imaging and statistical analysis of normal tissues and tumor tissues at 48 h post-injection of LS-HB, LS-HB@HvCeO$_2$, and LHCN1. Data were expressed as mean ± SD. D) The photoacoustic images of tumors in LHCN1 group at different time points post-injection. E) The in vivo PA images of sO$_2$ signals of tumor at LHCN1 pre-injection, 6 and 12 h post-injection.

accumulation of LHCN1. To further study the O$_2$-generating capability of LHCN1 in the tumor, we analyzed the O$_2$ saturation (sO$_2$) of the tumor using the PA imaging system. As shown in Figure 6E, at 12 h after intravenously injected LHCN1, the signal intensity of oxyhemoglobin was overwhelmingly higher than that at pre-injection and 6 h post-injection, which was consistent with fluorescence imaging results. Meanwhile, according to the PA signal intensity analysis, the average sO$_2$ at 12 h post-injection was 3.5- and 3.7-fold higher than that at 6 h post-injection and pre-injection, respectively (Figure S8, Supporting Information). Collectively, these results indicated that LHCN1 efficiently supplied O$_2$ to tumor tissues.

2.7. In Vivo Antitumor Effect of LHCN1

To investigate the in vivo effect of PDT of LHCN1, tumor-bearing mice were randomly divided into five groups (PBS, Only Laser, HCN1, LS-HB + Laser, LHCN1 + Laser; $n = 4$ per group). The tumors in the LS-HB + Laser and LHCN1 + Laser group were subjected to the laser irradiation (660 nm, 100 J cm^{-2}) after 12 h post-injection. As shown in **Figure 7**A, the tumor growths were significantly inhibited in the LHCN1 + Laser group. In contrast, the tumors in the PBS group, only laser group, and HCN1 group gradually enlarged. According to statistical analysis (Table S2, Supporting Information), the progressive growth of tumors in the

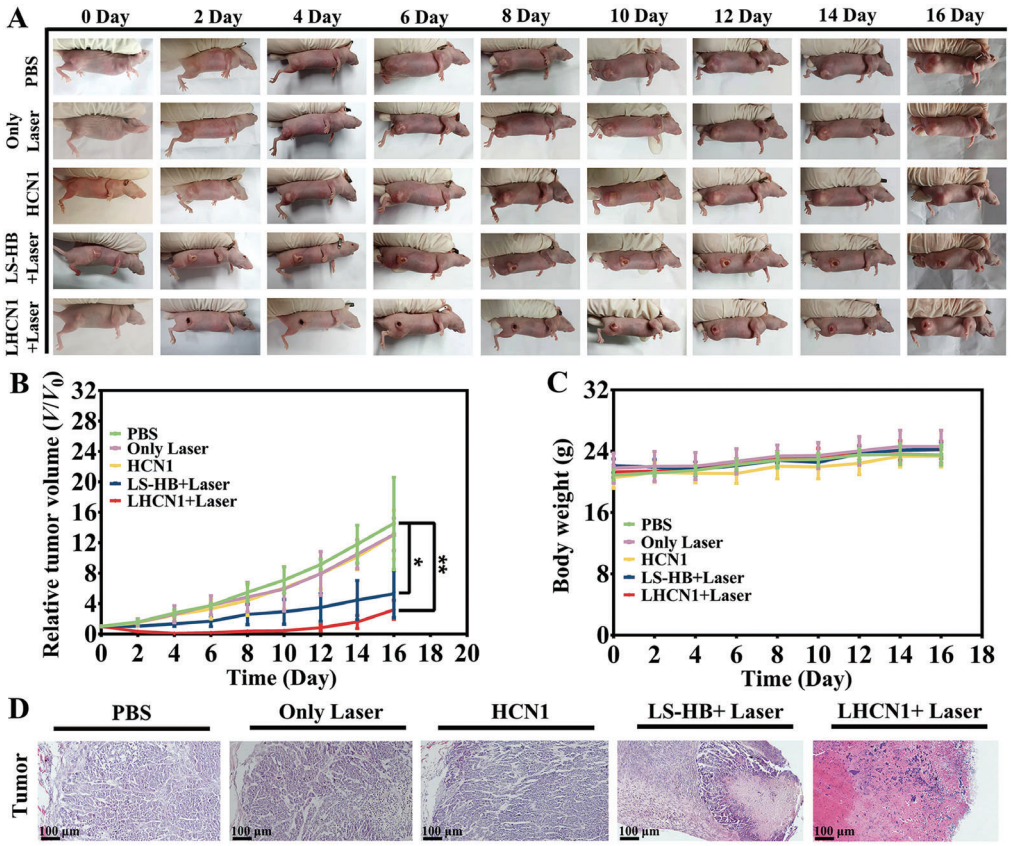

Figure 7. In vivo antitumor effect of LHCN1. A) Representative photographs of tumor-bearing mice on the 0th, 2nd, 4th, 6th, 8th, 10th, 12th, 14th, and 16th day after various treatment. B) Relative tumor volume (V/V_0) from different groups versus time (mean ± SD, $n = 4$, $^*p < 0.05$, $^{**}p < 0.01$). C) Body weight of tumor-bearing mice in each group after various treatment (mean ± SD, $n = 4$). D) H&E staining of tumors in each group after different treatments. Scale bar: 100 μm.

PBS, HCN1, and only laser group were further certified. In addition, the average relative tumor volume of LHCN1 + Laser group was 3.178 compared with those of the PBS (14.534) and LS-HB + Laser groups (5.28) on the 16th day post-treatment (Figure 7B). The results demonstrated that the PDT of LHCN1 had a particularly conspicuous antitumor efficiency. Furthermore, as shown in Figure S9, Supporting Information, compared with the average tumor weight (1.231 g) in the PBS group that in the LHCN1 + Laser group had an average tumor weight of 0.292 g, further confirming that PDT of LHCN1 could effectively inhibit the tumor growth. Haematoxylin and eosin (H&E) staining analysis showed that the tumor tissues had large area of apoptotic and necrotic areas, including blue-stained nuclear fragments, disintegrated matrices, swollen and liquefied collagen fibers in the interstitial tissue fused with necrotic cells into the red-stained unstructured material after LHCN1 + Laser treatment, and a partial apoptotic and necrotic area in the LS-HB + Laser group (Figure 7D). Taken together, the therapeutic effect of LHCN1 guiding PDT on oesophageal cancer is relatively apparent. Finally, statistical analysis indicated that there were no notable changes in the body weight of tumor-bearing mice after 16 days (Figure 7C), confirming that the in vivo systemic toxicity of LHCN1 in PDT was negligible.

2.8. In Vivo Safety Assessment of LHCN1

To explore the function of various organs, the blood of tumor-bearing mice in each group was collected for routine blood and biochemical tests after the 16 days of treatments. In the LHCN1 + Laser group, the routine blood indices, including red blood cell (RBC), white blood cell (WBC), lymphocytes (Lymph), monocytes (Mon), neutrophils (Gran), and platelet (PLT) counts, percentages of lymphocytes (Lymph%), monocytes (Mon%), and neutrophils (Gran%), haemoglobin (HGB), mean corpuscular volume (MCV), mean corpuscular hemoglobin (MCH), and mean corpuscular haemoglobin concentration (MCHC) were within normal ranges. Similarly, the biochemical indices, including alanine transaminase (ALT), aspartate transaminase (AST), direct bilirubin (DBIL), total bilirubin (TBIL), blood urea nitrogen (BUN), creatinine (CREA), and uric acid (UA), were within the normal range (**Figure 8**A,B; Tables S3 and S4, Supporting Information). After 16 days of treatments, H&E staining studies was used to evaluate the pathological changes in the tumors, the main organs (heart, liver, spleen, lung, kidney, and brain), and normal tissues (skin and muscle). No apparent abnormalities, such as lesions, necrosis, and fibrosis, were observed in the tissues and main organs of the LHCN1 + Laser group (Figure 8C). From the

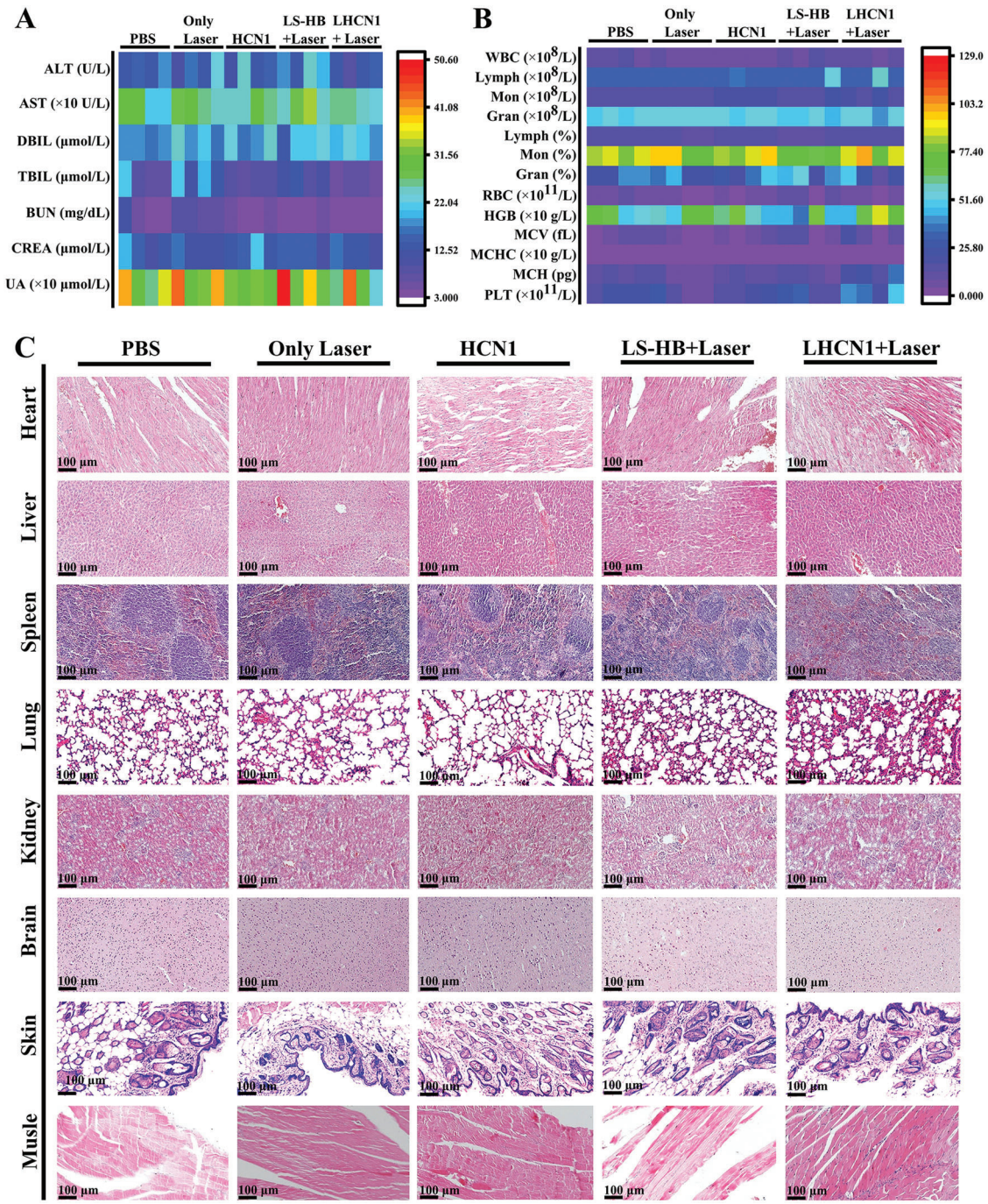

Figure 8. In vivo biosafety assessment of LHCN1. A,B) The hepatic and renal functions exponential index and the routine blood analysis of tumor-bearing mice from different groups on the 16th day post-treatment (mean ± SD, $n = 4$). C) H&E staining of the normal tissues and organs of nude mice after different treatment. Scale bar: 100 μm.

above results, it could be found that the PDT of LHCN1 had high biosafety and low biological toxicity in vivo.

3. Conclusion

In this study, a novel nano-system (LHCN1) comprising hollow virus-like mesoporous $HvCeO_2$ nanoparticles with high-efficiency LS-HB loading and surface NRP1 mAb decoration was successfully prepared to intensify PDT via tumor-targeted LS-HB delivery and O_2 self-supply in tumors. Owing to NRP1 mAb specific targeting, LHCN1 could efficiently accumulate within the tumor sites and was rapidly endocytosed into cells. Subsequently, hollow $HvCeO_2$ decomposed the intracellular endogenous H_2O_2 to produce O_2 via the valence transformation between Ce^{4+} and

Ce^{3+}, relieving the hypoxic tumor microenvironment to improve the PDT efficacy. Under NIR laser irradiation, LS-HB efficiently generated large amounts of ROS in cells. And then, ROS destroyed the mitochondria and leaded to mass tumor cells necrosis and apoptosis. Moreover, the in vivo results demonstrated that the PDT of LHCN1 could efficiently inhibit tumor growth and, importantly, exhibited negligible in vivo toxicity. In addition, LHCN1 could be used as a fluorescence and photoacoustic imaging contrast agent, which played the role of in the in vivo localization of drugs. Therefore, our LHCN1 nano-system is a promising strategy for imaging-guided tumor-specific precise treatment.

4. Experimental Section

Materials: LS-HB was obtained from Haining Lvsheng Pharmaceutical Technology Co., Ltd. (Haining, China). CTAB, TEOS, and APTES were purchased from Sigma-Aldrich (St. Louis, MO, USA). Sodium hydroxide and cyclohexane were obtained from Shanghai Chemical Co., Ltd. (Shanghai, China). $Ce(NO_3)_3{\cdot}6H_2O$ (99.95%) was purchased from Shanghai McLean Biochemical Technology Co., Ltd. (Shanghai, China). Urotropine (≥99.5%) was purchased from Aladdin Biotechnology Co., Ltd. (Shanghai, China). The CCK-8, Calcein AM/PI staining and H_2O_2 kits were purchased from Yeasen Biotechnology Co., Ltd. (Shanghai, China). The Hoechst-33258 staining and ROS detection kits (DCFH-DA) were purchased from Beyotime Biotechnology Co., Ltd. (Shanghai, China). The H&E staining solution kit was purchased from Nanjing Jiancheng Bioengineering Research Institute (Nanjing, China). The JC-1 mitochondrial membrane potential kit was purchased from MedChemExpress (Monmouth Junction, NJ, USA). RBITC was purchased from Sangon Biotechnology Co., Ltd. (Shanghai, China). MMP-2 cells were purchased from Shanghai Aiyan Biotechnology Co., Ltd. (Shanghai, China). Het-1a cells were obtained from the Cancer Research Center of Xiamen University (Xiamen, China). Female BALB/c nude mice (18-23 g, 7 weeks old) were purchased from Xiamen University Experimental Animal Co., Ltd. (Xiamen, China).

Preparation of VMSi: VMSi nanoparticles were synthesized using TEOS as a silica source and CTAB as a surfactant. First, 0.75 g CTAB was added into a round-bottom flask containing 60 mL of ultrapure water, dissolved by ultrasound, heated in an oil bath pot at 60 °C, and stirred. Thereafter, 0.75 mL of 0.1 mol L^{-1} NaOH solution was added, followed by 20 mL of a TEOS and cyclohexane mixture. After bathing for 48–72 h, the mixture was centrifuged at 10 000 rpm for 10 min, and the precipitate was collected and washed for several times.

Synthesis of $HvCeO_2$: $HvCeO_2$ nanoparticles were synthesized using the hard template method. Briefly, 10 mL of a 10 mg mL^{-1} VMSi nanoparticles suspension was mixed in a round-bottom flask containing 50 mL of ultrapure water and then dispersed by ultrasound (KQ-300DE, Kunshan Ultrasonic Instrument Co., Ltd, Kunshan, China). Next, the mixture was placed in an oil bath pot with magnetic stirring at 90 °C, and 0.18 g $Ce(NO_3)_3{\cdot}6H_2O$ was added after the temperature of the mixture increased to 90 °C, after which 0.105 g urotropine was added. After a night, the mixture was centrifuged at 5000 rpm for 10 min. Finally, the precipitate was collected and washed for several times.

Preparation of LHCN1: First, the surface of $HvCeO_2$ nanoparticles was aminated, and then NRP1 mAb with the activated carboxyl group activated by EDC and NHS was modified on the surface of $HvCeO_2$-NH_2. Finally, LHCN1 nanoparticles were synthesized by loading with LS-HB. Briefly, 5 mL of a 10 mg mL^{-1} $HvCeO_2$ nanoparticles suspension was added into a round-bottom flask containing 45 mL of ethanol, dispersed the mixture evenly, and placed in an oil bath pot with stirring (at 75 °C). After the temperature of the mixture reached 75 °C, 1 mL of APTES solution was mixed into the contents of the oil bath pot. After a night, the precipitate was collected to prepare HCN1. Next, 10 mg NRP1 mAb was added into a round-bottom flask containing 50 mL of ultrapure water and slowly stirred, and then 100 mg EDC and 40 mg NHS were added to the reaction system. Afterward, 50 mg $HvCeO_2$-NH_2 was added into the flask, the mixture was slowly stirred for 1 h, and the precipitate collected after 12 h. To synthesis of LHCN1, 50 mg of the prepared HCN1 was weighed into a round-bottom flask containing 50 mL of ultrapure water and evenly dispersed. After a night, 10 mg LS-HB was added into the flask, and the precipitate was collected and washed until the supernatant became transparent after centrifugation.

Characterization: The nanoparticles size and appearance were observed and analyzed using SEM (Zeiss GeminiSEM 500; Carl Zeiss Microscopy GmbH, Jena, Germany) and TEM (Leica EM TP, Germany). EDS (Talos F200s, FEI Corporation, Hillsboro, Oregon, USA) was used to analyze nanoparticle the elemental distribution and composition. The pore diameter and the specific surface area of the nanoparticles were determined using an automatic specific surface area and porosity analyzer (BET, Micromeritics ASAP 2460; Micromeritics Instrument Corporation, Norcross, GA, USA). The morphology of CeO_2 was determined by XRD (X'Pert Pro MPD; Panalytical Corporation, Netherlands). And the zeta potential was measured using a Malvern Zetasizer Nano ZS90 instrument (Malvern Panalaytical Ltd., Malvern, USA). The particle size distribution of LHCN1 was determined using DLS analyzer (Malvern Zetasizer Nano ZS90). The infrared spectra of the nanoparticles were obtained using FTIR (Vertex 70 V; Bruker Corporation, Germany). The valence states of CeO_2 were analyzed using XPS (Thermo Scientific Escalab 250Xi; USA). A Cary 5000 UV–vis NIR spectrophotometer (Agilent Technologies, Santa Clara, CA, USA) was used to analyze the UV absorption and visible spectrum of the nanodrugs and LS-HB loading. The RBITC fluorescein-labeled NRP1 mAb loading was analyzed by fluorescence spectrophotometer (Cary Eclipse; Varian, Inc., USA).

The Catalase-Mimetic Activity of LHCN1: Based on previous reports, CeO_2 could decompose H_2O_2 to produce O_2.[13b,18b] To investigate the catalase-mimetic activity of LHCN1, 2 μM H_2O_2 were added to 1 mL of solution (containing 40, 80, 120 μg mL^{-1} $HvCeO_2$, 40 μg mL^{-1} HCN1, and 40 μg mL^{-1} LHCN1, respectively). An H_2O_2 content detection reagent was used to treat the reaction solutions after incubation for 30 min, and then the absorbance was measured at 415 nm using an ultraviolet spectrophotometer (Varioskan Flash; Thermo Fish Scientific Corporation, USA). To research the effect of different pHs on the catalase-mimetic activity of $HvCeO_2$, the same method was used to determine the absorbance after H_2O_2 reacted with 120 μg mL^{-1} $HvCeO_2$ for 0, 10, 20, 30, 60, 90, and 120 min in pHs 7.4, 6.5, and 5.5, respectively. Finally, the results were subjected to statistical analysis.

Detection of Intracellular O_2 Production: To confirm that CeO_2 increased O_2 in cells, $[Ru(dpp)_3]Cl_2$ was used to determine intracellular O_2 production. Briefly, MMP-2 cells were seeded in 35 mm confocal dishes with 1×10^4 cells, and divided into the control, $HvCeO_2$, and LHCN1 groups. After incubation for 24 h, 40 μg mL^{-1} $HvCeO_2$ and 40 μg mL^{-1} LHCN1 were added to each group and incubated for 6 h, respectively. The cells were further incubated for 4 h after $(Rudpp_3)Cl_2$ staining. The results were visualized using a CLSM (Nikon A1R; Nikon Corporation, Tokyo, Japan).

Cellular Uptake and Specific Targeting Assay: To explore the endocytosis and targeting of LHCN1, LS-HB and RBITC were used as fluorescence probes, and NRP1 mAb was labeled with RBITC. MMP-2 cells were inoculated in 35 mm confocal dishes with 1×10^4 cells and incubated for 24 h. Thereafter, the fresh medium containing DMEM (containing 40 μg mL^{-1} LHCN1 or 40 μg mL^{-1} LHCN1-RBITC) was added. The fluorescence distributions were observed using a CLSM after incubation for 0, 0.5, 1, 3, 6, and 12 h. For the targeting experiment, the confocal dishes were divided into the $HvCeO_2$, NRP1 mAb, and LHCN1 groups ($HvCeO_2$, NRP1 mAb, and LHCN1 labeled by RBITC, respectively), and MMP-2 cells were inoculated into the corresponding 35 mm confocal dishes. After MMP-2 cells were cultured in the confocal dishes for 24 h, $HvCeO_2$-RBITC, NRP1 mAb-RBITC, and LHCN1-RBITC were used to treat MMP-2 for 0.5 h. Finally, the fluorescence was detected using a CLSM.

Cytotoxicity and Apoptosis Assays: The oesophageal cancer MMP-2 cells were inoculated into 96-well plates with 1×10^4 cells per well containing high-glucose DMEM culture medium, and they were divided into the control, only laser, drugs (HCN1, LS-HB, LHCN1), and drug + laser groups (HCN1 + 5 J cm^{-2} laser, LS-HB + 5 J cm^{-2} laser, and LHCN1 + 5 J

cm^{-2} laser). After 24 h of incubation, the corresponding drugs (2.5, 5, 10, 20, 40, and 80 μg mL^{-1} HCN1; 0.35, 0.7, 1.4, 2.8, 5.6, and 11.2 μg mL^{-1} LS-H; 2.5, 5, 10, 20, 40, and 80 μg mL^{-1} LHCN1 respectively containing 0.35, 0.7, 1.4, 2.8, 5.6, and 11.2 μg mL^{-1} LS-HB) were added into each group and incubated for 6 h. MMP-2 cells were cultured for 24 h after laser irradiation treatment. After the CCK-8 was co-incubated with the cells for 1 h, the absorbance of each well was measured at 450 nm using microplate reader (Bio-Rad Model 680; Bio-Rad Corporation, Hercules, California, USA). The cell viabilities of MMP-2 cells were measured using the same method after cells were treated respectively with NRP1 mAb (0.175, 0.35, 0.7, 1.4, 2.8, 5.6, 11.2 μg mL^{-1}), HCN1 (2.5, 5, 10, 20, 40, 80 μg mL^{-1}), LS-HB (0.35, 0.7, 1.4, 2.8, 5.6, 11.2 μg mL^{-1}), and LHCN1 (2.5, 5, 10, 20, 40, 80 μg mL^{-1}) without laser irradiation. To investigate the toxicity of LHCN1 to human normal oesophageal epithelial cells (Het-1a), Het-1a cells were treated with LHCN1 for 12 or 24 h after they were inoculated into 96-well plates at a density of 1×10^4 cells per well in RPMI 1640 culture medium. Subsequently, absorbance was measured using a microplate reader after CCK-8 staining, and cell viability was calculated based on the absorbance values.

To determine MMP-2 cell apoptosis after different treatments, an Annexin V-FITC/PI kit was used to detect the early and late apoptotic cells in the cell population. Briefly, MMP-2 cells were seeded into 6-well plates at a density of 1×10^5 cells per well, after which they were divided into the control, only laser, drugs (HCN1, LS-HB, and LHCN1), and drug + laser groups (HCN1 + 5 J cm^{-2} laser, LS-HB + 5 J cm^{-2} laser, and LHCN1 + 5 J cm^{-2} laser). Thereafter, MMP-2 cells were incubated with an apoptosis detection reagent (Annexin V-FITC/PI) after the corresponding treatment. Finally, flow cytometry was used to determine the apoptosis rates.

Based on the ability of the fluorescent probes (calcein AM/PI) to stain live and dead cells, confocal microscopy fluorescence images showed green and red fluorescence, respectively. Briefly, MMP-2 cells were inoculated into 35 mm confocal dishes at 1×10^4 cells per well and divided into the control, only laser, drugs (HCN1, LS-HB, and LHCN1), and drug + laser groups (HCN1 + 5 J cm^{-2} laser, LS-HB + 5 J cm^{-2} laser, and LHCN1 + 5 J cm^{-2} laser). Calcein AM/PI stained MMP-2 in each confocal dish after different treatments. The treated cells were imaged using a CLSM.

Determination of Mitochondrial Membrane Potential Changes and Intracellular ROS Production: Mitochondrial membrane potential changes, as a marker of early apoptosis, could be determined using JC-1 reagent. When the mitochondrial membrane potential was high, JC-1 aggregates in the matrix of mitochondria and formed a polymer that showed red fluorescence. When the mitochondrial membrane potential was low, JC-1 cannot aggregate in the mitochondria matrix and, as a monomer, showed green fluorescence. Accordingly, MMP-2 cells were inoculated into confocal dishes at 1×10^4 cells per well and divided into the control, only laser, drug (40 μg mL^{-1} LHCN1), and drug + laser group (40 μg mL^{-1} LHCN1 + 5 J cm^{-2} laser). After subjecting the MMP-2 cells to the different treatments and staining with JC-1, the results were visualized using a CLSM.

In cells, the fluorescent probe DCFH-DA was hydrolyzed by esterase into DCFH, which was oxidized to fluorescent DCF by intracellular ROS. Hence, DCF fluorescence reflected ROS levels. To verify the effect of LHCN1 on ROS, MMP-2 cells were seeded in 35 mm confocal dishes and 6-well plates at a density of 1×10^4 cells per well, respectively. The cells were stained and incubated for 20 min with DCFH-DA after different treatments. Thereafter, the cells in 6-well plates were collected for counting and fluorescence intensity analysis using flow cytometry (CytoFLEX; Beckman Coulter Corporation, Bria, California, USA) and ROS distribution in cells was observed using a CLSM.

In Vivo Fluorescence and Photoacoustic Imaging: The oesophageal tumor models were established by subcutaneous injection of MMP-2 cells (1×10^6 cells per mouse) into the back of the root of the right hind limb of nude mice. Until the tumor volumes of mice reached the appropriate size, tumor-bearing nude mice were randomly divided into the LS-HB, LS-HB@$HvCeO_2$, and LHCN1 groups (three mice in each group). Next, using caudal vein injection, the tumor-bearing nude mice were administered 100 μL of 0.14 mg mL^{-1} LS-HB, 100 μL of 1 mg mL^{-1} HB-$HvCeO_2$, or 100 μL of 1 mg mL^{-1} LHCN1 (all three containing the same amount of LS-HB), respectively. Following LS-HB imaging at 660 nm excitation luminescence, the fluorescence distribution of drugs in tumor-bearing nude mice was observed by an animal fluorescence in vivo imaging system (IVIS Lumina III; PerkinElmer Co., Waltham, Massachusetts, USA) at 1, 3, 6, 12, 24, and 48 h post-injection. The tumor sites of mice were imaged using a Vevo-LAZR-X PA imaging system (FUJIFILM VisualSonics, Toronto, ON, Canada) at 1, 3, 6, 12, 24, and 48 h following LHCN1 administration. Tumor sO_2 was determined using the PA imaging system before intravenous LHCN1 injection and at 6 and 12 h post-injection.

In Vivo Evaluation of Therapeutic Effect: To establish oesophageal tumor models, 1×10^6 MMP-2 cells were injected subcutaneously into per nude mice. When the tumor volumes of mice reached ≈100–200 mm^3, tumor-bearing nude mice were randomly divided into six groups (four mice in each group): PBS, only laser, HCN1, LS-HB + Laser, and LHCN1 + Laser groups. The nude mice were administered 100 μL of 1 × PBS buffer, 100 μL of 1.42 mg mL^{-1} HCN1, 100 μL of 0.2 mg mL^{-1} LS-HB, and 100 μL of 1.42 mg mL^{-1} LHCN1 (containing 0.2 mg mL^{-1} LS-HB) by caudal vein injection, respectively. Then, subcutaneous tumors in the laser, LS-HB + Laser, and LHCN1 + Laser groups were subjected to the laser irradiation at 660 nm and a laser dose density of 100 J cm^{-2}. After 12 h post-injection, the weight and tumor volumes of the nude mice in each group were measured on days 0, 2, 4, 6, 8, 10, 12, 14, and 16 post-treatment, and the tumors were simultaneously photographed and recorded. The following formula used to analyze the tumor relative volume (RV; *L*: the length, *W*: representing the width, V_0: the tumor volume on the 0th day):

$$\frac{(L \times W^2)}{2V_0} \tag{1}$$

In Vivo Biosafety Assessment: In vivo safety can be reflected by routine blood, the hepatic, and renal function exponential indices, and pathological changes in various tissues and organs. The heart, liver, spleen, lung, kidney, brain, tumor, skin, and muscle tissues of every tumor-bearing nude mouse in each group (PBS, only laser, LHCN1, LS-HB + Laser, HCN1 + Laser, and LHCN1 + Laser groups) were dissected, and whole blood and serum were collected. Whole-blood and serum samples from each group were determined for routine blood and liver and kidney function. Meanwhile, the obtained tissues were dehydrated and embedded, and pathological sections were prepared. The sections were then stained with H&E, scanned, and observed using a digital section-scanning system (Motic VM1; Motic Corporation).

All animal experiments were approved by the Xiamen University Ethics Committees (XMULAC20170297).

Statistical Analysis: All results were reported as the "mean ± SD." The GraphPad Prism (version 6.0; GraphPad Software, San Diego, CA, USA) was used for the statistical analysis. Significance was determined using Student's *t*-test analyze for the statistics from two groups and one-way analysis of variance (ANOVA) for the statistics from multiple groups. $*p < 0.05$, $**p < 0.01$, $***p < 0.001$, $****p < 0.0001$ represented statistical significance.

All data were not pre-processed except for H_2O_2 concentration post-treatment, the tumor volumes that were normalized for the evaluation of the catalase-like activity, and the in vivo antitumor effect of LHCN1, respectively. Moreover, the authors used one-way ANOVA to analyze the catalase-like activity of LHCN1, apoptosis rate, ROS generation, and in vitro PDT effect of different concentrations of LHCN1 and LS-HB ($n = 3$). Additionally, one-way ANOVA was applied to compare in vivo O_2 supply before and after LHCN1 injection, the weight of tumors after different treatments, and the volumes of tumors after different treatment ($n = 4$).

Supporting Information

Supporting Information is available from the Wiley Online Library or from the author.

Acknowledgements

The authors are grateful for the financial support from the National Natural Science Foundation of China (61905248 and 62005284), the Provincial Public Welfare Project of Fujian Province (2021R1001001, 2023R1001002, and 2023R1001003), and the Youth Innovation Foundation of Xiamen City (3502Z20206084). Meanwhile, the authors thank Haining Lvsheng Pharmaceutical Technology Co., Ltd for providing the LS-HB.

Conflict of Interest

The authors declare no conflict of interest.

Data Availability Statement

Research data are not shared.

Keywords

chlorin e6-C-15-ethyl ester, hollow virus-like CeO_2 nanoparticles, NRP1 monoclonal antibody, oxygen self-supply, photodynamic therapy

Received: September 21, 2022
Revised: November 17, 2022
Published online: December 12, 2022

[1] a) M. Ethirajan, Y. Chen, P. Joshi, R. K. Pandey, *Chem. Soc. Rev.* **2011**, *40*, 340; b) S. Kwiatkowski, B. Knap, D. Przystupski, J. Saczko, E. Kedzierska, K. Knap-Czop, J. Kotlinska, O. Michel, K. Kotowski, J. Kulbacka, *Biomed. Pharmacother.* **2018**, *106*, 1098; c) X. Li, J. F. Lovell, J. Yoon, X. Chen, *Nat. Rev. Clin. Oncol.* **2020**, *17*, 657.

[2] a) C. Donohoe, M. O. Senge, L. G. Arnaut, L. C. Gomes-da-Silva, *Biochim. Biophys. Acta, Rev. Cancer* **2019**, *1872*, 188308; b) K. F. Ferri, G. Kroemer, *Nat. Cell Biol.* **2001**, *3*, E255; c) L. Li, D. Song, L. Qi, M. Jiang, Y. Wu, J. Gan, K. Cao, Y. Li, Y. Bai, T. Zheng, *Cancer Lett.* **2021**, *520*, 143.

[3] R. D. Almeida, B. J. Manadas, A. P. Carvalho, C. B. Duarte, *Biochim. Biophys. Acta* **2004**, *1704*, 59.

[4] K. Sztandera, M. Gorzkiewicz, B. Klajnert-Maculewicz, *Wiley Interdiscip. Rev.: Nanomed. Nanobiotechnol.* **2020**, *12*, e1509.

[5] M. Lan, S. Zhao, W. Liu, C. S. Lee, W. Zhang, P. Wang, *Adv. Healthcare Mater.* **2019**, *8*, 1900132.

[6] M. Tavakkoli Yaraki, B. Liu, Y. N. Tan, *Nano-Micro Lett.* **2022**, *14*, 123.

[7] a) F. M. Shen, CN 103833762 A, **2014**; b) D. Y. Xu, F. M. Shen, CN 103396419 A, **2013**; c) L. Wang, L. Wang, Y. Zhang, Z. Zhao, C. Liu, M. Li, J. Liu, S. Wang, D. Yang, F. Luo, J. Yan, *Mol. Pharmaceutics* **2022**, *19*, 2607; d) C. Liu, T. Wu, S. Wang, W. Zhou, Y. Li, X. Chen, W. Li, Z. Huang, T. Li, L. Yang, P. Xu, J. Liuzong, J. Xie, D. Yang, J. Yan, F. Luo, *Photodiagn. Photodyn. Ther.* **2020**, *30*, 101718.

[8] Y. Sun, D. Zhao, G. Wang, Y. Wang, L. Cao, J. Sun, Q. Jiang, Z. He, *Acta Pharm. Sin. B* **2020**, *10*, 1382.

[9] a) X. Li, F. Luo, S. Wang, E. Ni, X. Tang, H. Lv, X. Chen, L. Chen, J. Yan, *Hybridoma* **2011**, *30*, 369; b) M. Alattar, A. Omo, M. Elsharawy, J. Li, *Eur. J. Cardio-Thorac. Surg.* **2014**, *45*, 514; c) D. E. Hansel, R. E. Wilentz, C. J. Yeo, R. D. Schulick, E. Montgomery, A. Maitra, *Am. J. Surg. Pathol.* **2004**, *28*, 347; d) Y. Ding, J. Zhou, S. Wang, Y. Li, Y. Mi, S. Gao, Y. Xu, Y. Chen, J. Yan, *Exp. Ther. Med.* **2018**, *16*, 537; e) F. Zeng, F. Luo, S. Lv, H. Zhang, C. Cao, X. Chen, S. Wang, Z. Li, X. Wang, X. Dou, Y. Dai, M. He, Y. Zhang, H. Lv, J. Yan, Y. Chen, *Anticancer Drugs* **2014**, *25*, 663.

[10] a) J. Deng, F. Liu, L. Wang, Y. An, M. Gao, Z. Wang, Y. Zhao, *Biomater. Sci.* **2018**, *7*, 429; b) X. Li, M. Gao, K. Xin, L. Zhang, D. Ding, D. Kong, Z. Wang, Y. Shi, F. Kiessling, T. Lammers, J. Cheng, Y. Zhao, *J. Controlled Release* **2017**, *260*, 12; c) X. Zhang, Q. Yan, D. N. Mulatihan, J. Zhu, A. Fan, Z. Wang, Y. Zhao, *Nanotechnology* **2018**, *29*, 255101; d) K. X. Teng, L. Y. Niu, Y. F. Kang, Q. Z. Yang, *Chem. Sci.* **2020**, *12*, 488.

[11] a) M. Li, Y. Shao, J. H. Kim, Z. Pu, X. Zhao, H. Huang, T. Xiong, Y. Kang, G. Li, K. Shao, J. Fan, J. W. Foley, J. S. Kim, X. Peng, *J. Am. Chem. Soc.* **2020**, *142*, 5380; b) Y. Wan, L. H. Fu, C. Li, J. Lin, P. Huang, *Adv. Mater.* **2021**, *33*, 2103978; c) J. Zhang, Z. Li, L. Liu, L. Li, L. Zhang, Y. Wang, J. Zhao, *Int. J. Nanomed.* **2022**, *17*, 1971.

[12] X. Meng, J. Deng, F. Liu, T. Guo, M. Liu, P. Dai, A. Fan, Z. Wang, Y. Zhao, *Nano Lett.* **2019**, *19*, 7866.

[13] a) C. P. Liu, T. H. Wu, C. Y. Liu, K. C. Chen, Y. X. Chen, G. S. Chen, S. Y. Lin, *Small* **2017**, *13*, 1700278; b) C. Yao, W. Wang, P. Wang, M. Zhao, X. Li, F. Zhang, *Adv. Mater.* **2018**, *30*, 1704833; c) S. Xu, X. Zhu, C. Zhang, W. Huang, Y. Zhou, D. Yan, *Nat. Commun.* **2018**, *9*, 2053.

[14] a) L. Gao, K. Fan, X. Yan, *Theranostics* **2017**, *7*, 3207; b) X. Liu, L. Yan, H. Ren, Y. Cai, C. Liu, L. Zeng, J. Guo, A. Liu, *Biosens. Bioelectron.* **2020**, *165*, 112342.

[15] a) X. M. Ma, Y. Cheng, H. Jian, Y. L. Feng, Y. Chang, R. X. Zheng, X. Q. Wu, L. Wang, X. Li, H. Y. Zhang, *Adv. Healthcare Mater.* **2019**, *11*, 33725; b) S. Zhao, H. X. Duan, Y. L. Yang, X. Y. Yan, K. L. Fan, *Nano Lett.* **2019**, *19*, 8887; c) C. Zhang, W. B. Bu, D. L. Ni, S. J. Zhang, Q. Li, Z. W. Yao, J. W. Zhang, H. L. Yao, Z. Wang, J. L. Shi, *Angew. Chem., Int. Ed.* **2016**, *55*, 2101; d) X. Ma, Y. Cheng, H. Jian, Y. Feng, Y. Chang, R. Zheng, X. Wu, L. Wang, X. Li, H. Zhang, *Adv. Healthcare Mater.* **2019**, *8*, 1900256; e) L. E. Gevers, L. R. Enakonda, A. Shahid, S. Ould-Chikh, C. I. Q. Silva, P. P. Paalanen, A. Aguilar-Tapia, J. L. Hazemann, M. N. Hedhili, F. Wen, J. Ruiz-Martinez, *Nat. Commun.* **2022**, *13*, 2960; f) Y. Wang, Z. Tan, Z. Zhang, P. Zhu, S. W. Tam, Z. Zhang, X. Jiang, K. Lin, L. Tian, Z. Huang, S. Zhang, Y. K. Peng, K. K. L. Yung, *ACS Appl. Mater. Interfaces* **2022**, *14*, 35423; g) N. Feng, Y. Liu, X. Dai, Y. Wang, Q. Guo, Q. Li, *RSC Adv.* **2022**, *12*, 1486.

[16] a) J. T. Dahle, Y. Arai, *Int. J. Environ. Res. Public Health* **2015**, *12*, 1253; b) R. Zamiri, H. A. Ahangar, A. Kaushal, A. Zakaria, G. Zamiri, D. Tobaldi, J. M. F. Ferreira, *PLoS One* **2015**, *10*, e0131851.

[17] C. Xu, X. G. Qu, *NPG Asia Mater.* **2014**, *6*, e90.

[18] a) E. G. Heckert, A. S. Karakoti, S. Seal, W. T. Self, *Biomaterials* **2008**, *29*, 2705; b) T. Pirmohamed, J. M. Dowding, S. Singh, B. Wasserman, E. Heckert, A. S. Karakoti, J. E. King, S. Seal, W. T. Self, *Chem. Commun.* **2010**, *46*, 2736.

[19] a) T. Pirmohamed, J. M. Dowding, S. Singh, B. Wasserman, E. Heckert, A. S. Karakoti, J. E. S. King, S. Seal, W. T. Self, *Chem. Commun.* **2010**, *46*, 2736; b) X. Liu, J. Liu, S. Chen, Y. Xie, Q. Fan, J. Zhou, J. Bao, T. Wei, Z. Dai, *J. Mater. Chem. B* **2020**, *8*, 9933.

[20] a) X. Luo, J. Xie, Z. Zhou, S. Ma, L. Wang, M. Li, J. Liu, P. Wang, Y. Li, F. Luo, J. Yan, *ACS Appl. Mater. Interfaces* **2021**, *13*, 44013; b) W. Wang, P. Wang, X. Tang, A. A. Elzatahry, S. Wang, D. Al-Dahyan, M. Zhao, C. Yao, C. T. Hung, X. Zhu, T. Zhao, X. Li, F. Zhang, D. Zhao, *ACS Cent. Sci.* **2017**, *3*, 839.

[21] J. Yue, Y. Shen, L. Liang, L. Cong, W. Xu, W. Shi, C. Liang, S. Xu, *Anal. Chem.* **2020**, *92*, 6081.

[22] Z. J. L. Liu, P. Y. Wang, F. Xie, J. H. Chen, M. M. Cai, Y. Li, J. H. Yan, Q. Lin, F. H. Luo, *Adv. Healthcare Mater.* **2022**, *11*, 2102060.